Ultrasonics 137 (2024) 107166

Contents lists available at ScienceDirect

Ultrasonics

journal homepage: www.elsevier.com/locate/ultras

Thorough ultrasonic rheology of soft, visco-elastic materials: Example of crosslinked Polyurethane elastomer

Quentin Baudis, Tony Valier-Brasier, Régis Wunenburger *

Sorbonne Université, CNRS, Institut Jean Le Rond d'Alembert, UMR 7190, 4 Place Jussieu, Paris, F-75005, France

A B S T R A C T

We present a thorough procedure for measuring the rheological properties of soft, highly attenuating, visco-elastic materials at ultrasonic frequencies. The material chosen for this illustration is a crosslinked Polyurethane (PU) elastomer (*Sika* UR3440 type), which is widely used in the field of underwater acoustics. We determine its complex longitudinal modulus M and shear modulus G as function of frequency in the range 1–5 MHz and of temperature in the range 5–40 °C. M is determined from the measurement of the transmission of longitudinal, plane waves by a slab of PU immersed in water. G is determined by contact measurements from the transmission and reflection of transverse, plane waves by a slab of PU. This determination of G for such a soft and viscous material as PU is made possible by the use of thin slabs and the implementation of an original signal analysis. M, G and bulk modulus K are found to obey the time–temperature superposition principle and to be accurately described by a fractional derivative rheological model. This allows us to propose analytic formulas for the frequency and temperature dependence of M, G and K valid above PU glass transition temperature.

1. Introduction

The main purpose of this work is to establish a procedure for thoroughly determining the rheological properties, namely the complex longitudinal modulus M and shear modulus G of soft, visco-elastic materials as function of temperature and frequency in the ultrasonic frequency range.

The material chosen for illustrating this procedure is a crosslinked Polyurethane (PU) elastomer (UR3440 from *Sika*), which is widely used in the field of underwater acoustics as anechoic coating [1,2] due to its impedance matching with water [3–5] and good resistance to high pressure, low temperatures and aging. Characterizing this specific elastomer is indeed the secondary purpose of this work. The determination of the visco-elastic properties of PU is indeed crucial for designing elastic metamaterials for underwater applications [6], since both longitudinal and transverse waves are involved in the wave scattering and attenuation processes at play in metamaterials.

The rheological properties of polymeric materials can be determined in a wide frequency range by combining several measurement techniques working in distinct frequency ranges [7,8] or by using a single technique and exploiting the time–temperature superposition (TTS) principle [9]. We briefly go through them and point their limitations for highly attenuating materials such as PUs. (i) Dynamic mechanical analysis (DMA) performed in the low frequency range ($f < 10$ kHz) and at controlled temperature can give access to G and Young modulus $E = G(3M - 4G)/(M - G)$ of PUs in wide frequency ranges using the TTS principle [10–13]. (ii) The measurement of the transmission of longitudinal, plane waves by an immersed slab of visco-elastic material, called hereafter the immersion technique, gives access to M in the ultrasonic frequency range [14,15], even for highly attenuating materials. The measurement of the reflection of longitudinal, plane waves by a slab of liquids through direct contact can give also access to M in the ultrasonic frequency range [16–18]. Discrepancies are found between measurements obtained by DMA and the immersion technique, especially concerning the dissipative part of the visco-elastic moduli [19–21]. (iii) The ultrasonic technique based on longitudinal–transverse wave conversions at the material–liquid interfaces of an immersed sample irradiated by a plane, longitudinal wave beyond the critical angle [22], which has been applied to viscoelastic materials, cannot be applied to highly attenuating media such as PUs [23]. (iv) The technique based on the measurement of the reflection of a transverse ultrasonic wave by an interface between a solid and a visco-elastic liquid at normal [24–26], oblique [27,28] or grazing incidence [29,30], called hereafter the reflection technique, can also be applied to solid, visco-elastic materials [31]. Discrepancies are also found between measurements obtained by DMA and the reflection technique [31]. (v) Finally, the technique based on the modification of the impedance of a piezo-electric transducer by an adherent layer of visco-elastic, weakly dissipative solid can also give simultaneously access to M and G [32]. To conclude this review, up to now the only technique giving access to the shear modulus G of highly attenuating materials at ultrasonic frequencies was the reflection technique, which often lacks precision especially regarding the dissipative part of G. In this article we combine the immersion technique for accessing the longitudinal modulus M of

* Corresponding author.
E-mail address: regis.wunenburger@sorbonne-universite.fr (R. Wunenburger).

https://doi.org/10.1016/j.ultras.2023.107166
Received 20 July 2022; Received in revised form 22 June 2023; Accepted 14 September 2023
Available online 27 September 2023

soft, highly attenuating, visco-elastic materials at ultrasonic frequencies and a reflection–transmission technique, called hereafter the sandwich technique, for accessing their shear modulus G in the same frequency range. The latter technique was recently developed by our team for accessing the shear modulus G of viscous liquids at ultrasonic frequencies [33]. It was adapted to soft, highly attenuating materials for the purpose of this work. More precisely, the determination of G for such a soft and viscous material as PU was made possible by the use of thin slabs and the implementation of an original signal analysis which is detailed hereafter.

The article is structured as follows. In Section 2, we present the main features of the immersion technique and the measurements of longitudinal velocity and attenuation of PU. In Section 3, we present the main features of the sandwich technique, how it was adapted to soft materials and the measurements of transverse velocity and attenuation of PU. In Appendix A, we quantify its repeatability. In Appendix B, we study the influence of the hardening temperature on the PU visco-elastic properties. Interestingly, the sandwich technique can also be used to monitor the PU polymerization process, as detailed in Appendix C. In Section 4, we present the TTS principle and demonstrate that the complex longitudinal and shear moduli M and G as well as the complex longitudinal modulus $K = M - 4/3\,G$ satisfy the TTS principle by determining the corresponding scaling factors. In Section 5, we demonstrate that M, G and K are accurately described by a fractional derivative model and we provide analytic formulas for the frequency and temperature dependence of M, G and K valid above PU glass transition temperature $T_g < -60\,°\text{C}$.

2. Measurement of longitudinal velocity and attenuation

2.1. Experimental setup and protocol

PU samples used in this study are obtained by solidifying a mixture of liquid polymer and liquid hardener provided separately. Immediately after blending, the mixture is degassed at ambient temperature in order to release air bubbles. Then it is poured into a cylindrical mold. PU crosslinking leading to its hardening is achieved in 4 h in an incubator at 80 °C. The sample thickness is $h_a = (10.37 \pm 0.03)$ mm and its diameter is $D = (129.10 \pm 0.13)$ mm at ambient temperature $T_a = (16.4 \pm 0.1)\,°\text{C}$. Mass density of crosslinked PU at T_a is $\rho_a = (1017 \pm 5)$ kg m^{-3}.

The sample is fixed in a tapped panel and is immersed in a 900 mm × 400 mm × 360 mm tank of water. Two identical *NDT Systems* IBHG024-type longitudinal wave transducers ($2a = 0.5$ inch active diameter, 2.25 MHz nominal central frequency) are precisely aligned along the sample axis and oriented parallel to the sample faces using goniometers and translation stages (see inset of Fig. 2), so that the sample is irradiated at normal incidence.

Except during the short intervals of acoustic measurements, water is constantly agitated in order to avoid density stratification above the heat exchanger of the thermal regulation circuit located at the bottom of the caulked tank. Measurements are performed at controlled temperature ranging between 5 °C and 45 °C, as measured using a Platinum resistance thermometer. Temperature variations during a measurement are in the range of 20 mK, while temperature gradients at the tank scale are insignificant.

The emitting transducer is fed with pulses by a *Olympus* PR5072-type pulser-receiver at a 100 Hz repetition rate. The signals detected by the receiving transducer are acquired and digitized with a 14-bit resolution at $f_s = 400$ MHz sampling frequency and averaged over 1000 acquisitions.

The longitudinal wave phase velocity c_L and attenuation α_L in PU are determined by comparing the wave transmitted through the sample with the wave transmitted through water only in absence of sample. The accuracy of the technique relies on the precise knowledge of the wave velocity in water c_w. Thus, c_w is accurately determined before each transmission measurement by translating the emitter along the wave propagation axis using a motorized translation stage and by measuring the slope of the linear variation of the pulse travel time through water versus the emitter–receiver distance. The temperature dependence of c_w, shown in Fig. 1, agrees with Medwin's model of acoustic velocity in water that takes into account water temperature, salinity S (best fit value $S = 1.4$ ppm) and immersion depth [34].

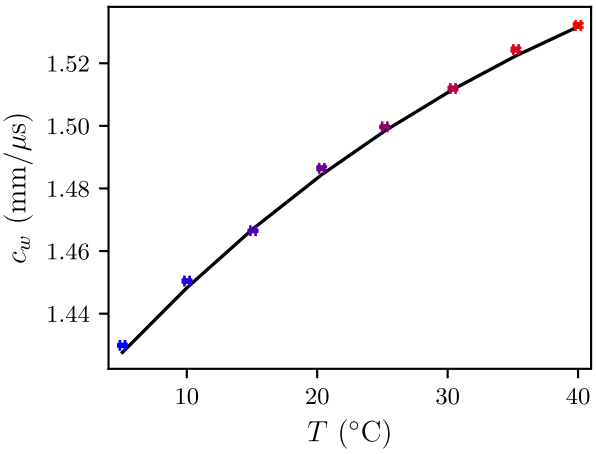

Fig. 1. Temperature dependence of acoustic velocity c_w in tank water. Symbols with error bars: measurements. Solid curve: Medwin's model [34].

2.2. Signal analysis and results

The transmission coefficient of the PU slab is defined as the ratio between the Fourier transform $\hat{S}(f)$ of the time signal transmitted through the PU sample $S(t)$ and the Fourier transform $\hat{S}_w(f)$ of the time signal transmitted through water only in absence of sample $S_w(t)$ (see inset of Fig. 2). Since PU impedance matches that of water within 5%, we can safely neglect the reflections at PU–water interfaces and the round trips of the wave inside the slab. Thus, $\hat{S}/\hat{S}_w = \mathcal{T}\exp[-i\,(k_L - k_w)\,h]$, where $k_w = \omega/c_w$ is the real wavenumber in water assuming negligible attenuation in water ($\omega = 2\pi f$), $k_L(\omega) = \omega/c_L(\omega) - i\alpha_L(\omega)$ the unknown complex acoustic wavenumber in PU, and

$$\mathcal{T} = \frac{4\rho_w k_w \rho k_L}{\left(\rho_w k_L + \rho k_w\right)^2} \tag{1}$$

the product of pressure transmission coefficients at water–PU and PU–water interfaces with ρ_w the mass density of water [35]. Thus,

$$\begin{cases} c_L = c_w + \dfrac{\omega h}{\arg\left(\hat{S}/\hat{S}_w\right) - \arg\left(\mathcal{T}\right)}, \\ \alpha_L = \dfrac{1}{h}\log\left(\left|\mathcal{T}\right|\left|\hat{S}/\hat{S}_w\right|\right). \end{cases} \tag{2}$$

where log is the natural logarithm and h the sample thickness [14]. The temperature dependence of ρ_w is evaluated from [36]. A linear approximation can be used for evaluating the variation of ρ and of h with temperature:

$$h(T) = h_a\left[1 + \kappa\left(T - T_a\right)\right] \tag{3}$$

$$\rho(T) = \rho_a\left[1 - 3\kappa\left(T - T_a\right)\right] \tag{4}$$

where $\kappa = 2.60\times10^{-4}$ K^{-1} the PU linear expansion coefficient at ambient temperature [37].

Note that the problem is implicit since $\mathcal{T}$ depends on k_L which is unknown. Thus, c_L and α_L are determined by iteration at each investigated frequency.

The frequency range of validity of experimental determination of k_L is determined by requiring a minimum single-to-noise ratio for TTS analysis. This leads to apply a spectral cutoff at −20 dB of the signal

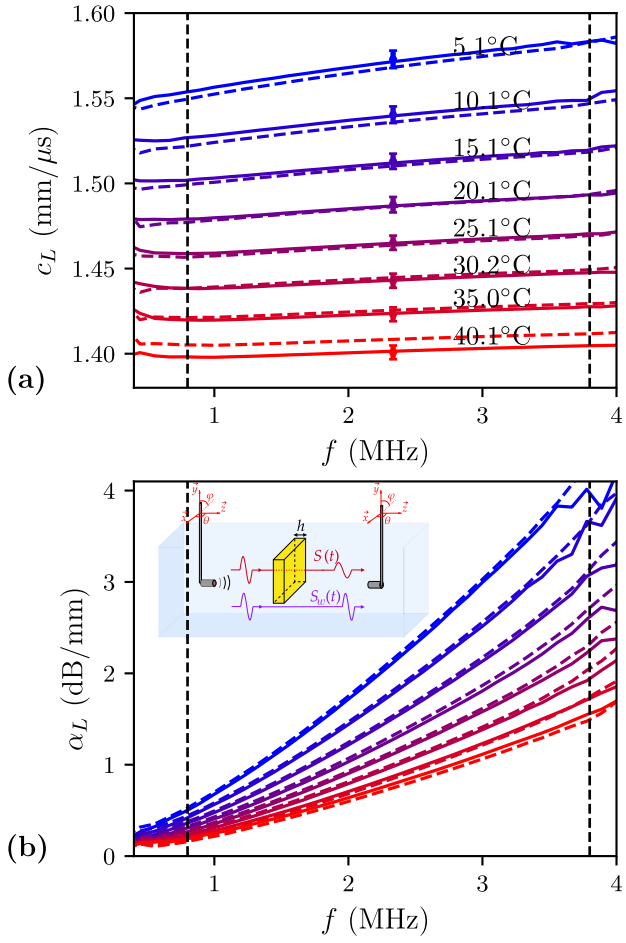

Fig. 2. (a) Phase velocity c_L and (b) attenuation α_L of longitudinal waves in polyurethane as function of frequency f for several temperatures. Vertical dashed lines correspond to $f_{\min}$ and $f_{\max}$, see text. Solid (resp. dashed) lines: sample with thickness $h_a = (10.50 \pm 0.03)$ mm (resp. $h_a = (9.84 \pm 0.03)$ mm). Inset: sketch of the experimental setup.

energy maximum. This leads to $f_{\min} = 0.8$ MHz and $f_{\max} = 3.8$ MHz. We checked that this frequency range satisfies two criteria:

- In order to avoid any propagation through the tapped panel, the beam (main diffraction lobe) diameter has to be smaller than the sample internal diameter D. The corresponding lower boundary for frequency is f_1 such that [34,38]

$$\arcsin\left(3.83/(k_w a)\right) = \arctan\left[(D/2 - a)\,/\,(L - z_R)\right]. \tag{5}$$

  Here, $f_1 = 0.44$ MHz at $T = 5$ °C and $f_1 = 0.47$ MHz at $T = 40$ °C.
- In order for the wave propagating through the sample to be considered as a plane wave, the sample has to be located in the far-field distance of emitter, namely z_R. The corresponding upper boundary for frequency is f_2 such that $z_R \simeq k_w a^2/2\pi = L$ [39]. For the transducers used in this study, $f_2 = 4.6$ MHz at $T = 5$ °C and $f_2 = 5.0$ MHz at $T = 40$ °C.

These two criteria are actually fulfilled since $f_{\min} > f_1$ and $f_{\max} < f_2$.

The variations of c_L and α_L versus f are displayed in Fig. 2 for several temperatures and for two samples with different thicknesses. c_L exhibits a weak dispersion and decreases with T. α_L increases with frequency f and decreases with temperature T.

3. Measurement of transverse velocity and attenuation

3.1. Experimental setup and protocol

The setup and experimental procedure used in this work for measuring the transverse velocity and attenuation are almost identical to the ones presented in [33]. We remind them for self-consistency purpose.

The setup is composed of two delay lines sandwiching a slab of PU, as sketched in Fig. 3(a). Basically, the transverse velocity and attenuation in PU are deduced from the transmission and reflection of shear waves by the slab.

Two identical delay lines made of 2017A Duralumin are used. Two Olympus V154 shear wave transducers with $f_c = 2.25$ MHz nominal central frequency, 0.5 inch active diameter and −6 dB frequency bandwidth, are tighten against each delay line using screws, see Fig. 3(a). Contact is ensured by using as couplant phenyl salicylate (Salol) instead of commercial shear wave couplant as in [33,40]. To do this, contact surfaces are wetted with liquid Salol heated above 60 °C, then pressed against each other. Ultimately, Salol solidifies by cooling though heat conduction. Noticeably, intimate contact between solid PU and delay lines is achieved by taking advantage of the liquid behavior of PU before hardening. Non-crosslinked PU mixture is poured on the top surface of the bottom delay line, then the liquid layer is squished between the delay lines separated by calibrated spacers. As a consequence, the sample thickness is equal to the spacer thickness h. Finally, the setup is put in a refrigerated incubator with controlled temperature $T_c = 5$ °C and PU crosslinking occurs, resulting in the adhesion of PU to the delay lines. The progress of the cross-linking process is monitored by acquiring on a regular basis the time-dependent transmitted signal. Its peak-to-peak amplitude A increases in time with the progress of the cross-linking process. When A saturates, the PU hardening process is assumed as achieved, the last acquired signals are considered as the steady-state signals, then the setup temperature can be possibly modified. The thermalization of the setup after a temperature change is achieved after 4 h.

On the one hand, the delay lines sandwiching the PU slab as sketched in Fig. 3(a), we measure (i) the signal $S_{R_A}(t)$ (resp. $S_{R_B}(t)$) emitted by transducer A (resp. B), reflected by PU slab and received by A (resp. B) and (ii) the signal $S_{T_A}(t)$ (resp. $S_{T_B}(t)$) emitted by transducer A (resp. B), transmitted by PU slab and received by B (resp. A). On the other hand, the setup being unmounted and the sample being removed as sketched in Fig. 3(b), we measure the calibration signal $S_{C_A}(t)$ (resp. $S_{C_B}(t)$) emitted by transducer A (resp. B), reflected by delay line free surface and received by A (resp. B). Typical reflected, transmitted ans calibration signals are shown in Fig. 4. Despite the use of rather thin samples (90 μm), the transmitted signal amplitude is strikingly small compared to that of the reflected signal (40 times smaller), as a consequence of the large impedance mismatch between Dural delay lines and PU but also of the large attenuation of shear waves in PU.

The slab transmission coefficient $\mathcal{T}^{\exp}$ and reflection coefficient $\mathcal{R}^{\exp}$ satisfy:

$$\begin{cases} (\mathcal{T}^{\exp})^2(\omega) &= \dfrac{\hat{S}_{T_A}(\omega)}{\hat{S}_{C_A}(\omega)}\dfrac{\hat{S}_{T_B}(\omega)}{\hat{S}_{C_B}(\omega)}, \\ \mathcal{R}^{\exp}(\omega) &= \dfrac{1}{2}\left(\dfrac{\hat{S}_{R_A}(\omega)}{\hat{S}_{C_A}(\omega)} + \dfrac{\hat{S}_{R_B}(\omega)}{\hat{S}_{C_B}(\omega)}\right) \end{cases} \tag{6}$$

where $\hat{S}(\omega)$ is the Fourier transform of $S(t)$ [33].

To conclude, the principle of measurement of the transverse velocity c_T and attenuation α_T is similar to that of c_L and α_L except that (i) water is replaced by solid delay lines and (ii) transmission through water only, which corresponds to the reference signal, is replaced by total reflection by the ends of unmounted delay lines.

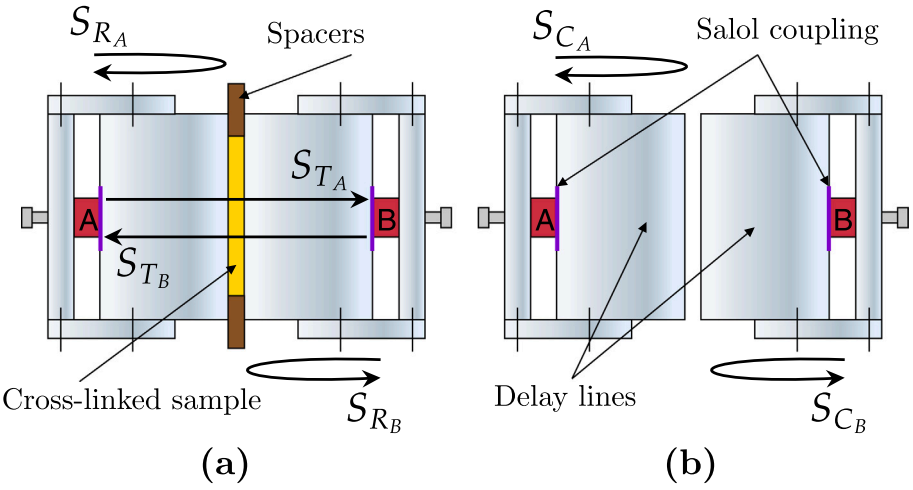

Fig. 3. Sketch of the experimental setup. *A*, *B*: shear wave transducers. (a) Reflected and transmitted signals measured using the mounted setup. (b) Calibration signals measured using the unmounted setup.

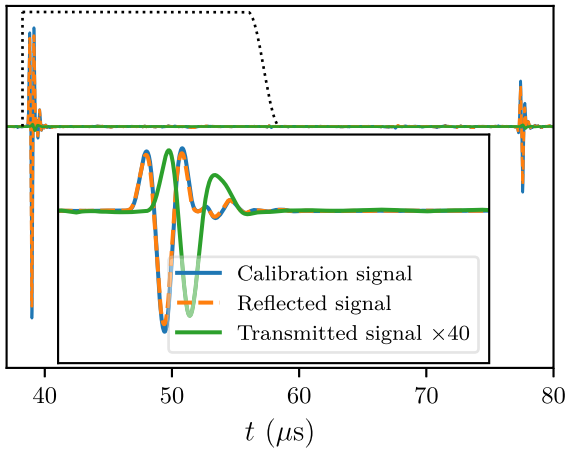

Fig. 4. Reflected, transmitted and calibration signals through a 90 μm thick PU slab irradiated by a shear pulse-like wave at f_c = 2.25 MHz central frequency and at temperature T = 5 °C. The dotted curve represents the asymmetric Tukey window applied to the signals. Inset: zoom on the signals. The transmitted signal is amplified 40 times.

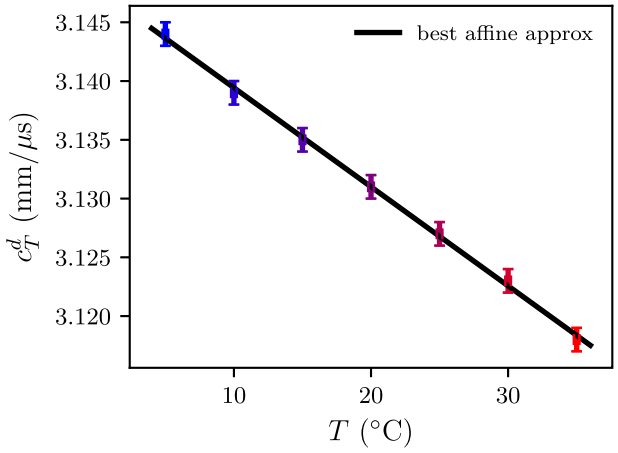

Fig. 5. Variation of the transverse velocity c_T^d in Duralumin versus temperature.

3.2. Signal analysis and propagation model

Signals are windowed in order to get rid of echoes having experienced a reflection on one transducer-delay line interface, allowing to consider the delay lines as infinitely long. More precisely, windowing is made spectrally smooth by using asymmetric Tukey windows, as illustrated in Fig. 4 [41]. Given the weakness of the transmitted signals, $f_{\min}$ = 1.2 MHz and $f_{\max}$ = 3.7 MHz are rather chosen according to a −10 dB criterium. Given the characteristic features of the transducers and the dimensions of the delay lines and sample, f_1 = 0.6 MHz and f_2 = 4.6 MHz. Here also $f_{\min}$ and $f_{\max}$ satisfy $f_{\min} > f_1$ and $f_{\max} < f_2$.

On the other hand, assuming (i) infinitely long delay lines and (ii) that the waves propagating back and forth though the sample and delay lines are plane waves, a 1D Fabry–Perot interferometer model adequately describes the reflection and transmission by the delay line-PU-delay line assembly, leading to the following theoretical expressions for the transmission coefficient $\mathcal{T}$th and the reflection coefficient $\mathcal{R}$th:

$$\begin{cases} \mathcal{T}^{\text{th}}(c_T, \alpha_T, \omega) &= \dfrac{t_{01}t_{10}e^{-ik_T h}}{1 + r_{01}r_{10}e^{-2ik_T h}} \\ \mathcal{R}^{\text{th}}(c_T, \alpha_T, \omega) &= r_{01} + \dfrac{t_{01}r_{10}t_{10}e^{-ik_T h}}{1 + r_{01}r_{10}e^{-2ik_T h}} \end{cases} \tag{7}$$

where 0 denotes the delay line, 1 the sample, r_{ij} and t_{ij} are respectively the stress reflection and transmission coefficients at an interface between i and j impinged from i and $k_T(\omega) = \omega/c_T(\omega) - i\alpha_T(\omega)$ is the complex transverse wave number in the sample.

It is worth, pointing out that the determination of k_T from $\mathcal{T}$th and $\mathcal{R}$th is not unique. In the next section, we detail the procedure allowing to determine the physically relevant value dispersion curve $k_T(\omega)$.

To end this subsection, we specify the temperature dependence of the quantities entering into Eq. (7). The delay lines are made of 2017A Duralumin, whose mass density at 20 °C is ρ_d = 2790 kg m^{-3}. Its thermal expansion, which is characterized by its linear expansion coefficient $\kappa = 2.3 \times 10^{-5}$ K^{-1}, results in a 0.24% variation of its mass density ρ_d and in a 0.08% variation of the length of the delay lines in the investigated temperature range. As shown in Fig. 5, the measured variation of the transverse velocity c_T^d in Duralumin in the investigated temperature range is 0.83%. The spacers are made of steel. Owing to its small linear expansion coefficient $\kappa \simeq 10^{-5}$ K^{-1}, the variation of the strip thicknesses in the investigated temperature range is 0.03%. Thus, we neglect their dilatation and we consider their nominal thickness h, which is provided by the calibration service with a ± 5 μm uncertainty.

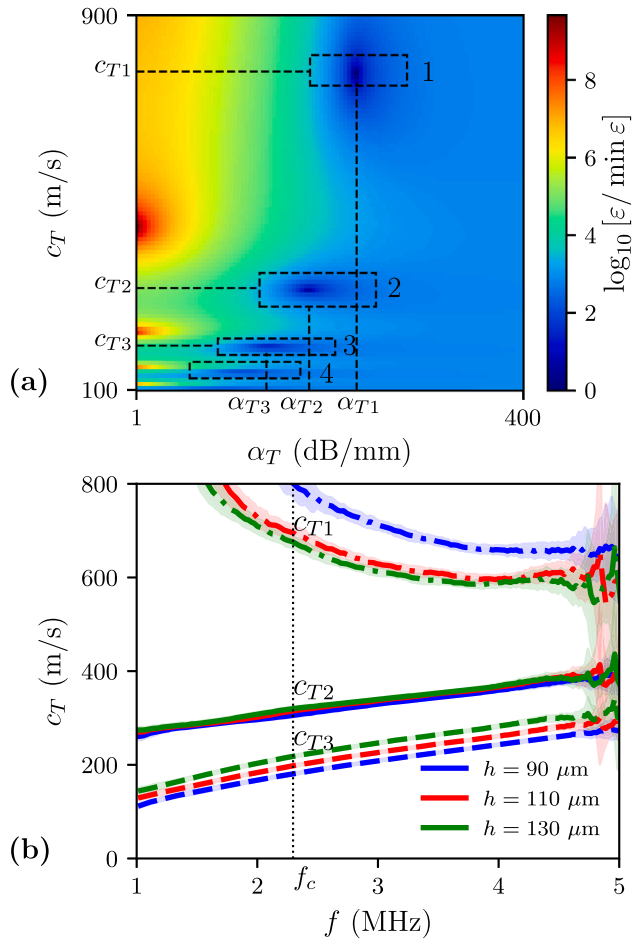

Fig. 6. (a) Variation (in color scale) of the decimal logarithm of the relative error $\log_{10}[\varepsilon/\min(\varepsilon)]$ defined by Eq. (8) as function of c_T and α_T for the 90 µm thick sample at central frequency f_c and temperature $T = 5$ °C. The dashed frames enclose the four minima. (b) Variations versus frequency of the values of c_T corresponding to the minima of $\varepsilon/\min(\varepsilon)$ number 1, 2 and 3 for three samples with different thicknesses at $T = 5$ °C.

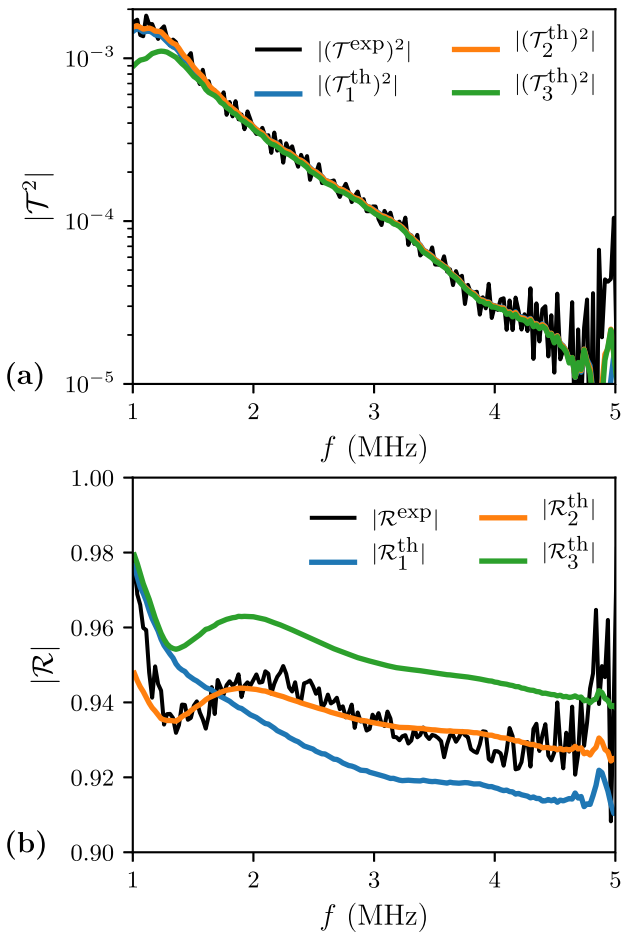

Fig. 7. (a) Variations versus frequency of the amplitude of the square of the experimental transmission coefficient $|(\mathcal{T}^{\exp})^2|$ and of its theoretical predictions $\left|(\mathcal{T}_1^{\text{th}})^2\right|$, $\left|(\mathcal{T}_2^{\text{th}})^2\right|$ and $\left|(\mathcal{T}_3^{\text{th}})^2\right|$, evidencing that $\mathcal{T}^2$ cannot be used to select the physically relevant dispersion curve. (b) Variations versus frequency of the experimental reflection coefficient $|\mathcal{R}^{\exp}|$ and of its theoretical predictions $\left|\mathcal{R}_1^{\text{th}}\right|$, $\left|\mathcal{R}_2^{\text{th}}\right|$ and $\left|\mathcal{R}_3^{\text{th}}\right|$, evidencing that $\mathcal{R}$ can be used to select the physically relevant dispersion curve and that $\{c_{T2}(\omega), \alpha_{T2}(\omega)\}$ is the only relevant dispersion branch.

3.3. Dispersion curve selection

In order to determine $k_T(\omega)$, for each investigated value of ω, we compute the 2D array of values of the error $\varepsilon(\omega)$ defined as [40]:

$$\varepsilon(\omega) = \left|(\mathcal{T}^{\text{th}})^2(c_T, \alpha_T, \omega) - (\mathcal{T}^{\exp})^2(\omega)\right|^2 \tag{8}$$

with c_T ranging from 100 m s^{-1} to 900 m s^{-1} and α_T ranging from 0 to 400 dB mm^{-1}. The variations of $\varepsilon/\min(\varepsilon)$ at $T = 5$ °C and $\omega = 2\pi f_c$ versus c_T and α_T is represented in color scale in Fig. 6(a). As a consequence of the periodic behavior of $\mathcal{T}$th with respect to $1/c_T$, four minima (numbered from 1 to 4) can be detected, whose coordinates correspond to four possible sets of values of c_T and α_T at $\omega = 2\pi f_c$, labeled c_{Ti} and α_{Ti}, $i = 1$ to 4. In order to select the physically relevant dispersion curve $\{c_T(\omega), \alpha_T(\omega)\}$, two approaches can be adopted: (i) measuring the reflection and transmission by several samples having different thicknesses, or (ii) selecting the dispersion curve that corresponds to the best fit of $\left|(\mathcal{T}^{\text{th}})^2\right|(\omega)$ and $\left|\mathcal{R}^{\text{th}}\right|(\omega)$ by Eq. (7). In the following, we implement the two approaches.

On the one hand, three samples with different thicknesses, namely $h = 90$ µm, 110 µm and 130 µm are measured. The variations versus frequency of c_{T1}, c_{T2} and c_{T3} measured in the three samples are shown in Fig. 6(b). Since $c_{T2}(\omega)$ is independent of h whereas both $c_{T1}(\omega)$ and $c_{T3}(\omega)$ depend on h, we conclude that $\{c_{T2}(\omega), \alpha_{T2}(\omega)\}$ is the only physically relevant dispersion branch.

On the other hand, we label $\left|(\mathcal{T}_i^{\text{th}})^2(\omega)\right|$ (resp. $\left|\mathcal{R}_i^{\text{th}}(\omega)\right|$) the values of $\left|(\mathcal{T}^{\text{th}})^2\right|$ (resp. $\left|\mathcal{R}^{\text{th}}\right|$) computed using the branch of possible solutions $\{c_{Ti}(\omega), \alpha_{Ti}(\omega)\}$, $i = 1$ to 3. As shown in Fig. 7(a), $\left|(\mathcal{T}_i^{\text{th}})^2\right|$ coincides with $\left|(\mathcal{T}^{\exp})^2\right|$ whatever i, which prevents us from selecting the physically relevant dispersion curve using $\mathcal{T}^2$. On the contrary, as shown in Fig. 7(b), $|\mathcal{R}^{\exp}|$ agrees with $\left|\mathcal{R}_i^{\text{th}}\right|$ only for $i = 2$, which allows us to select the physically relevant dispersion curve using $\mathcal{R}$ and leads us to confirm that $\{c_{T2}(\omega), \alpha_{T2}(\omega)\}$ is the only relevant dispersion branch.

Finally, we stress that here the physically relevant dispersion curve cannot be selected by evaluating the transverse wave velocity from the pulse time-of-flight through the sample, contrary to the case of less attenuating and thicker samples [40]. PU is indeed highly attenuating, which imposes the use of thin samples for measuring a transmitted signal. Consequently, the reflected and transmitted echoes interfere, which prevents us from measuring their time-of-flight. Thus, the comparison of $\mathcal{R}^{\exp}$ and of $\mathcal{R}$th appears as a valuable alternative to the measurement of the time-of-flight for selecting the physically relevant dispersion curve in thin samples using a single sample.

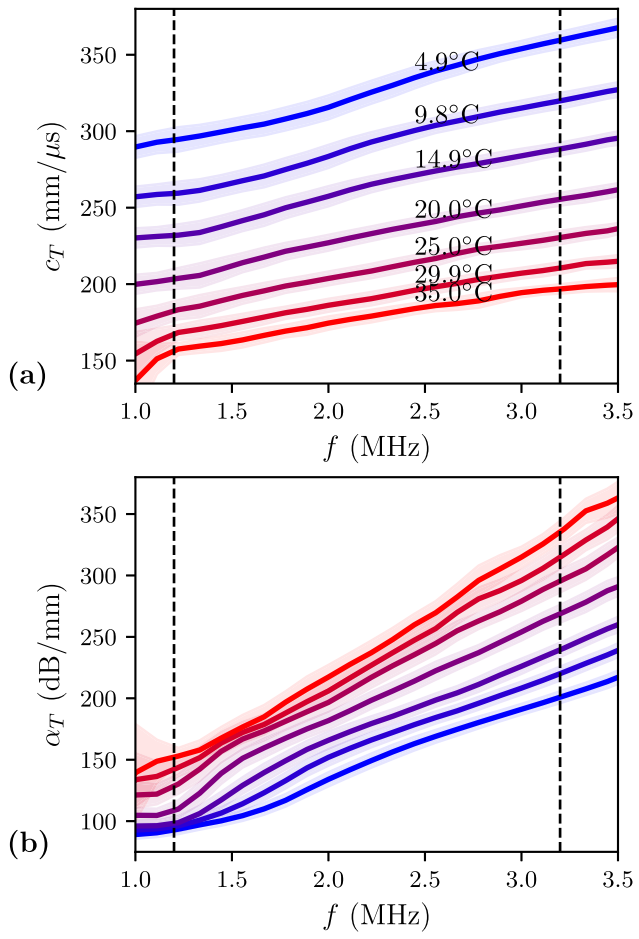

Fig. 8. (a) Phase velocity c_T and (b) attenuation α_T of transverse waves in polyurethane as a function of frequency f for several temperatures. Vertical dashed lines correspond to $f_{\min}$ and $f_{\max}$, see text. Excess thickness represents the uncertainty, which is computed as in [40].

3.4. Results

The variations versus f of c_T and α_T corresponding to the physically relevant dispersion curve are displayed in Fig. 8 for several temperatures. c_T exhibits a large dispersion and decreases with T. α_T increases with frequency f. Contrary to α_L, α_T increases with temperature T.

4. Exploiting the time–temperature superposition principle

The purpose of this section is to derive scaled expressions for M, G and K valid for any temperature above T_g by exploiting the time–temperature superposition principle.

4.1. Time–temperature superposition principle

PU is known to belong to the category of so-called thermorheologically simple polymers which obey the time–temperature superposition (TTS) principle [9], i.e. whose dynamic response is related to temperature by scaling relations. There exists two real scaling functions a_T and b_T^G such that the frequency dependence of G at temperature T, $G(f,T)$, is related to its frequency dependence at temperature T_{ref}, $G(f,T_{\text{ref}})$ through:

$$G(a_T(T,T_{\text{ref}})\,f,T_{\text{ref}}) = b_T^G(T,T_{\text{ref}})\,G(f,T) \tag{9}$$

On the one hand, above T_g, a_T generally satisfies the Williams–Landel–Ferry (WLF) equality [42,43]:

$$\log_{10}(a_T\,(T,T_{\text{ref}})) = -c_1(T_{\text{ref}})\frac{T-T_{\text{ref}}}{c_2(T_{\text{ref}})+T-T_{\text{ref}}}, \tag{10}$$

where $c_1(T_{\text{ref}})$ and $c_2(T_{\text{ref}})$ are two functions of T_{ref} which depend on the material.

On the other hand, according to Buech–Rouse's kinetic theory of polymers [44,45] and Doi–Edwards's [46] theory that extends the spectra of Buech–Rouse's theory, the variation of the shear relaxation modulus with temperature varies proportionally to ρT and b_T^G is predicted to satisfy:

$$b_T^G\,(T,T_{\text{ref}}) = \frac{\rho(T_{\text{ref}})}{\rho(T)}\frac{T_{\text{ref}}}{T} \tag{11}$$

where $\rho(T)$ is the material mass density at temperature T, which satisfies:

$$\rho(T) = \rho(T_{\text{ref}})\left[1-3\kappa\left(T-T_{\text{ref}}\right)\right]. \tag{12}$$

Given the typical value of κ for PUs, for $T_{\text{ref}} < T$, b_T satisfies $b_T(T,T_{\text{ref}}) < 1$.

An open question is whether Eqs. (9), (10), (11) also apply to M and K.

In the following, C denoting G, M or K, we use the following complex notation $C = C_1 + iC_2$ valid in the harmonic regime, C_1 being the storage modulus and C_2 the loss modulus.

4.2. Scaled expressions for M, G and K

To exploit the TTS principle, after choosing T_{ref}, we follow a three-steps process:

1. Since the measurements of M are the most regular, we determine the variation of $a_T(T,T_{\text{ref}})$ versus T from M_2/M_1 (as explained in [47]), then its best fit by Eq. (10).
2. We determine the variation of $b_T^M(T,T_{\text{ref}})$ versus T from M_1. On the other hand, we determine the variation of $b_T^G(T,T_{\text{ref}})$ versus T from G_1.
3. Finally, we evaluate K with $K = M - 4/3G$. We perform another determination of $a_T(T,T_{\text{ref}})$ from K_2/K_1 and we determine $b_T^K(T,T_{\text{ref}})$ versus T from K_1.

4.2.1. Determination of a_T

In order to extrapolate our measurements of M toward the low frequency domain, we choose $T_{\text{ref}} = 5$ °C, as explained below. We consider the variations versus frequency of M_2/M_1, which are shown in Fig. 9(a) for all the investigated temperatures numbered in ascending order T_i, $i = 1$ to 8. According to Eq. (9),

$$\frac{M_2}{M_1}(f,T) = \frac{M_2}{M_1}(a_T(T,T_{\text{ref}})\,f,T_{\text{ref}}) \tag{13}$$

As a consequence, for each temperature T_i we determine the value $a_T(T_i,T_{\text{ref}})$ of the scaling factor a_T ensuring that $M_2/M_1(f,T_i)$ coincides with $M_2/M_1(a_T(T_i,T_{\text{ref}})f,T_{\text{ref}})$ in their common frequency range. Practically, we determine by iteration the value $a_T(T_{i+1},T_{\text{ref}})$ such that the point of abscissa $a_T(T_{i+1},T_{\text{ref}})\,f_c$ and ordinate $M_2/M_1(f_c,T_{i+1})$ coincides with the point of abscissa $a_T(T_i,T_{\text{ref}})\,f_c$ and ordinate $M_2/M_1(f_c,T_i)$ with $a_T(T_1,T_{\text{ref}}) = 1$ since $T_1 = T_{\text{ref}}$. The resulting continuous behavior of M_2/M_1 versus $a_T f$ is shown in Fig. 9(b). The variation of $a_T(T,5°\text{C})$ versus T is shown in inset of Fig. 9(b).

Our choice for T_{ref} can now be justified. Since the frequency range of practical interest for underwater applications is typically 1 – 100 kHz, we aim to extrapolate the elastic moduli toward frequencies lower than the frequency range investigated in this work. Since M_2/M_1 decreases when temperature increases, as shown in Fig. 9(a), choosing for T_{ref} the lowest investigated temperature 5 °C results in $a_T(T,T_{\text{ref}}) < 1$ for $T > T_{\text{ref}}$, which allows us to extrapolate the visco-elastic moduli toward

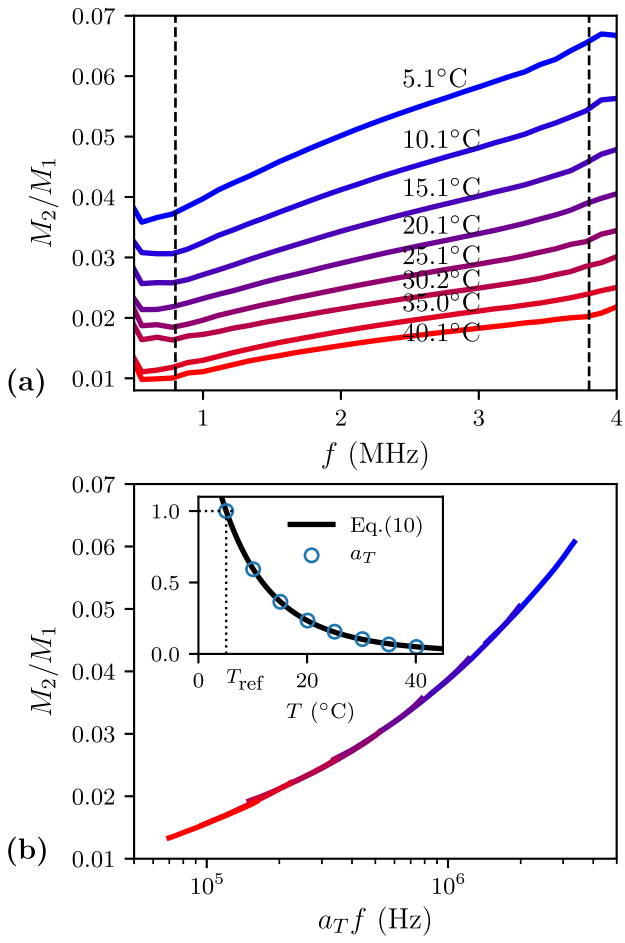

Fig. 9. (a) Variations versus frequency of M_2/M_1 for several temperatures T_i^M, $i = 1$ to 8. (b) Variation of M_2/M_1 versus scaled frequency $a_T(T, T_{\text{ref}})\, f$ with $T_{\text{ref}} = 5.1$ °C. Inset: variation of $a_T(T, T_{\text{ref}})$ versus T (symbols) and its best fit by WLF equation (10) (solid curve).

scaled frequencies $a_T f$ lower than the lowest investigated frequency using the TTS principle. If 40 °C was chosen as the reference temperature, we would be able to extrapolate the visco-elastic moduli toward frequencies higher than the frequency range investigated in this work.

Rearranging Eq. (10) leads to:

$$T - T_{\text{ref}} = -c_2 - c_1 \frac{T - T_{\text{ref}}}{\log_{10}(a_T)}, \tag{14}$$

so that the variation of $T - T_{\text{ref}}$ versus $(T - T_{\text{ref}}) / \log_{10}(a_T)$ is linear with slope $-c_1$ and intercept $-c_2$. c_1 and c_2 are determined that way and the resulting best fit of a_T by Eq. (10) is shown in inset of Fig. 9(b). The corresponding best fit values of c_1 and c_2 are given in Table 1. They can be compared to values of c_1 and c_2 for other PUs reported in the literature and given in Table 1 provided that the differences in reference temperature are taken into account. Indeed, since the values c_1^{litt} and c_2^{litt} reported in the literature are determined using other choices for the reference temperature $T_{\text{ref}}^{\text{litt}}$, they have to be transformed using the following equalities [10]:

$$c_1 = \frac{c_1^{\text{litt}} c_2^{\text{litt}}}{c_2^{\text{litt}} + T_{\text{ref}} - T_{\text{ref}}^{\text{litt}}}, \tag{15}$$

$$c_2 = c_2^{\text{litt}} + T_{\text{ref}} - T_{\text{ref}}^{\text{litt}} \tag{16}$$

so that they correspond to the reference temperature chosen in this study T_{ref}.

Table 1
Values of the coefficients entering WLF equality Eq. (10) defining a_T deduced from M and K. These values are compared to other experimental determinations of these coefficients reported in literature for three PUs, computed for the same reference temperature T_{ref}.

	From M	From K	Ref. [10]	Ref. [5]	Ref. [48]
T_{ref} (°C)	5.1	5.1	5.1	5.1	5.1
c_1	6.6	6.3	15.5	9.8	8.5
c_2 (K)	143.1	79.7	88.0	90.6	106.2

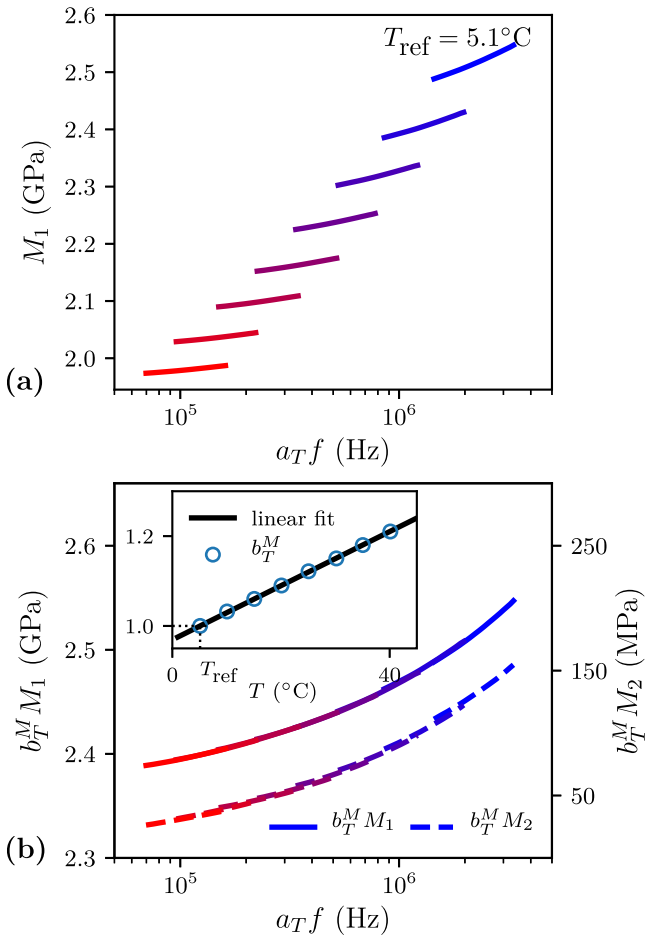

Fig. 10. (a) Variations of storage longitudinal modulus M_1 versus scaled frequency $a_T f$ for several temperatures T_i^M, $i = 1$ to 8 (same color convention as in Fig. 9(a)). (b) Variations of scaled storage and loss longitudinal moduli $b_T^M M_1$ (solid lines, left-hand vertical scale) and $b_T^M M_2$ (dashed lines, right-hand vertical scale) versus scaled frequency $a_T f$ with $T_{\text{ref}} = 5.1$ °C. Inset: experimental variation of $b_T^M(T, T_{\text{ref}})$ versus T (symbols) and its best linear fit (solid line).

As shown in Table 1, the measured c_1 and c_2 are close to those of other PUs. This is in line with the general observation that $c_1 \sim 10$ and $c_2 \sim 100$ K for PUs [42].

4.2.2. Determination of b_T^M and b_T^G

Determination of b_T^M. We consider the variations versus frequency of the storage modulus M_1 at several temperatures T_i^M, $i = 1$ to 8, which are shown in Fig. 10(a).

In order to determine the scaling factor b_T^M that would satisfy:

$$M(a_T(T, T_{\text{ref}})\, f, T_{\text{ref}}) = b_T^M(T, T_{\text{ref}})\, M(f, T) \tag{17}$$

we determine by iteration its value $b_T^M(T_{i+1}, T_{\text{ref}})$ such that the point of abscissa $a_T(T_{i+1}, T_{\text{ref}})\, f_c$ and ordinate $b_T^M(T_{i+1}, T_{\text{ref}}) M_1(f_c, T_{i+1})$ coincides with the point of abscissa $a_T(T_i, T_{\text{ref}})\, f_c$ and ordinate $b_T^M(T_i, T_{\text{ref}}) M_1(f_c, T_i)$ with $b_T^M(T_1, T_{\text{ref}}) = 1$ since $T_1 = T_{\text{ref}}$.

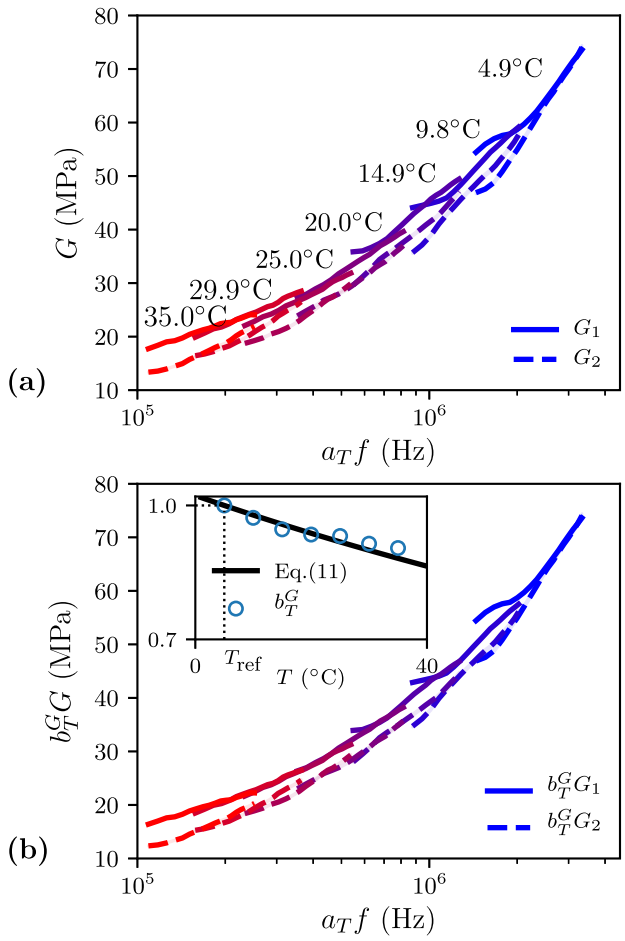

Fig. 11. (a) Variations of storage and loss shear moduli G_1 and G_2 versus scaled frequency $a_T f$ for several temperatures T_i^G, $i = 1$ to 7. (b) Variations of scaled storage and loss shear moduli $b_T^G G_1$ and $b_T^G G_2$ versus scaled frequency $a_T f$. Inset: experimental variation of $b_T^G(T, T_{ref})$ versus T with $T_{ref} = 5.1$ °C (symbols) and its theoretical prediction Eq. (11) (solid line).

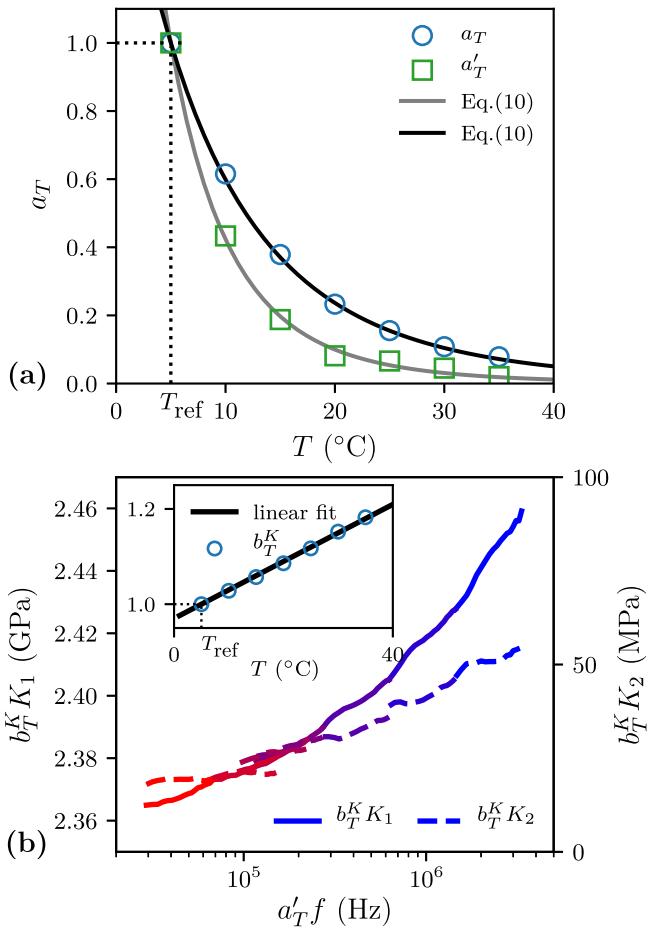

Fig. 12. (a) Squares: variation versus T of $a'_T(T, T_{ref})$ determined from K_2/K_1 with $T_{ref} = 5.1$ °C and its best fit by WLF equation (10) (solid curve). Circles: for comparison purpose, we display again the variation versus T of $a_T(T, T_{ref})$ determined from M_2/M_1 and its best fit by WLF equation (10) (bold solid curve). (b) Variation of scaled storage and loss bulk moduli $b_T^K K_1$ (solid lines, left-hand vertical scale) and $b_T^K K_2$ (dashed lines, right-hand vertical scale) versus scaled temperature $a'_T f$ with $T_{ref} = 5.1$ °C. Inset: experimental variation of $b_T^K(T, T_{ref})$ versus T and its best linear fit (solid line).

The resulting continuous behavior of $b_T^M M_1$ versus $a_T f$ is shown in Fig. 10(b). As shown in inset of Fig. 10(b), $b_T^M(T, T_{ref})$ increases linearly with T, whereas Eq. (11) predicts a decreasing behavior. The slope of the best linear fit of $b_T^M(T)$ is 6.07×10^{-3} K^{-1}.

As shown in Fig. 10(b), $b_T^M M_2$ also varies continuously with $a_T f$, which confirms the validity of Eq. (17) concerning M.

Determination of b_T^G. Now we consider the variations versus frequency of storage modulus G_1 and loss modulus G_2 at several temperatures T_i^G, $i = 1$ to 7, which are shown in Fig. 11(a). We note that G_1 and G_2 are close, which evidences the high attenuation of this PU and highlights the performances of the sandwich technique.

The scaling factor b_T^G as defined by Eq. (9) is determined from G_1 in the same manner as b_T^M.

The resulting continuous behavior of $b_T^G G_1$ versus $a_T f$ is shown in Fig. 11(b). As shown in inset of Fig. 11(b), the variation of $b_T^G(T, T_{ref})$ with T is quantitatively described by Eq. (11). Note that the variation of b_T^G with T as predicted by Eq. (11) is mainly due to the variation of T_{ref}/T. This may explain why previous measurements of G and Young's modulus E of PUs [10] led to fit b_T^G using the simplified relation $b_T^G(T, T_{ref}) = T_{ref}/T$.

As shown in Fig. 11(b), $b_T^G G_2$ also varies continuously with $a_T f$, which confirms the validity of Eq. (9) concerning G.

4.2.3. Other determination of a_T from K and determination of b_T^K

Since $T_i^M \simeq T_i^G$, $i = 1$ to 7, the bulk modulus K can be evaluated from the raw measurements of M and G assuming $K(T_i^M, f) = M(T_i^M, f) - 4/3\, G(T_i^G, f)$, $i = 1$ to 7.

Although K_2/K_1 evaluated at several temperatures T_i^M ($i = 1$ to 7) is observed to vary approximately continuously with the scaled temperature $a_T f$, a further optimization effort leads to note that K_2/K_1 is smoother when a_T is determined as in sub Section 4.2.1 by considering $f = 1.8$ MHz instead of f_c. The resulting variation versus temperature of this new determination of a_T called a'_T is plotted in Fig. 12(a). The discrepancy between a_T and a'_T can be considered as a assessment of the uncertainty of the determination of a_T. The best fit of a'_T by Eq. (10) is shown in Fig. 12(a) and the corresponding best fit values of c_1 and c_2 are given in Table 1.

Then we determine the scaling factor b_T^K that would satisfy:

$$K(a_T(T, T_{ref})\, f, T_{ref}) = b_T^K(T, T_{ref})\, K(f, T) \tag{18}$$

from K_1 following the procedure detailed in sub Section 4.2.2. The variation of b_T^K versus temperature T with $T_{ref} = 5.1$ °C is displayed in inset of Fig. 12(b). b_T^K increases linearly with T. We note that the slope 5.40×10^{-3} K^{-1} of its best linear fit is close to the slope 4.2×10^{-3} K^{-1} of the linear variation of b_T^K versus T of the PU studied in [5] which was determined by combination of DMA and longitudinal measurements.

Table 2
Values of the coefficients entering Eq. (19) fitted to M, G and K for the PU studied here.

C =	M	G	K
C_0 (MPa)	2335	4.23	2329
C_v (kPa s)	204.16	19.51	1231
α_C	0.422	0.503	0.280

The variation of scaled bulk modulus $b_T^K K$ versus scaled temperature $a'_T f$ with $T_{\text{ref}} = 5.1$ °C is displayed in Fig. 12(b). The continuous behaviors of $b_T^K K_1$ and $b_T^K K_2$ versus $a_T f$, shown in Fig. 12(b), confirms the validity of Eq. (18) concerning K.

Finally, we note that $b_T^K K_2 > 0$, which corresponds to the fulfillment of the passivity condition established by Norris for isotropic, linear, visco-elastic media [49].

5. Fractional derivative model

As shown in Fig. 13(a–c), $b_T^M M_2$, $b_T^G G_2$ and $b_T^K K_2$ behave as a power laws of $a_T f$ with exponent distinctly smaller than unity. Thus, a linear rheological model is not suitable for describing their viscoelastic behavior. As shown in Fig. 13(b), $b_T^G G_2$ actually behaves as a power law of $a_T f$ with exponent close to its theoretically predicted value 1/2 [42,44].

As proposed in [50], the use of fractional order derivatives is found to accurately describe the rheological behavior of polymers. Accordingly, in the harmonic regime, the complex modulus C ($C = M$, G or K) satisfies:

$$C(\omega) = C_0 + C_v (i\omega)^{\alpha_C}, \tag{19}$$

or equivalently:

$$C_1 = C_0 + C_v \cos\left(\frac{\pi}{2}\alpha_C\right)\omega^{\alpha_C} \tag{20}$$

$$C_2 = C_v \sin\left(\frac{\pi}{2}\alpha_C\right)\omega^{\alpha_C} \tag{21}$$

Regarding M, G and K, C_0 C_v and α are determined by optimization using Python *lmfit* library. The best fit values of C_0, α and C_v are shown in Table 2.

The resulting best fits of M, G and K by Eq. (19) are shown in Figs. 13(a-c). We conclude to a quantitative agreement between the measurements of M, G and K and the fractional Kelvin–Voigt model.

6. Conclusion and

This work constitutes a thorough study of the visco-elastic properties of a cross-linked PU in the ultrasonic frequency range resulting in the accurate determination of its longitudinal and shear moduli as a function of temperature above glass transition temperature and of frequency. This could be achieved by analyzing both the reflection and transmission of longitudinal and transverse waves by slabs of PU and by applying the TTS principle. A fractional derivative rheological model could be successfully fitted to the scaled bulk and shear moduli.

The techniques and methods presented in this article can be considered as generic for characterizing the rheology of soft, visco-elastic materials. Softer materials (i.e. materials with smaller G_1) can be considered but the smaller G_1, the smaller the transmission coefficient as the result of the larger impedance contrast between the sample and the delay lines, and consequently the smaller the signal-to-noise ratio (SNR) of the transmitted signal. To overcome this, the samples can be made thinner, however the control of the flatness and parallelism of the delay line surfaces is more crucial. Another material constituting the delay lines can also be considered for this purpose. For example PMMA (plexiglas) would result in a reduction of the shear wave impedance of the delay line by a factor 5, but the large attenuation (of the order of 100 m^{-1} in the MHz frequency range) would result in a decrease of the SNR [40].

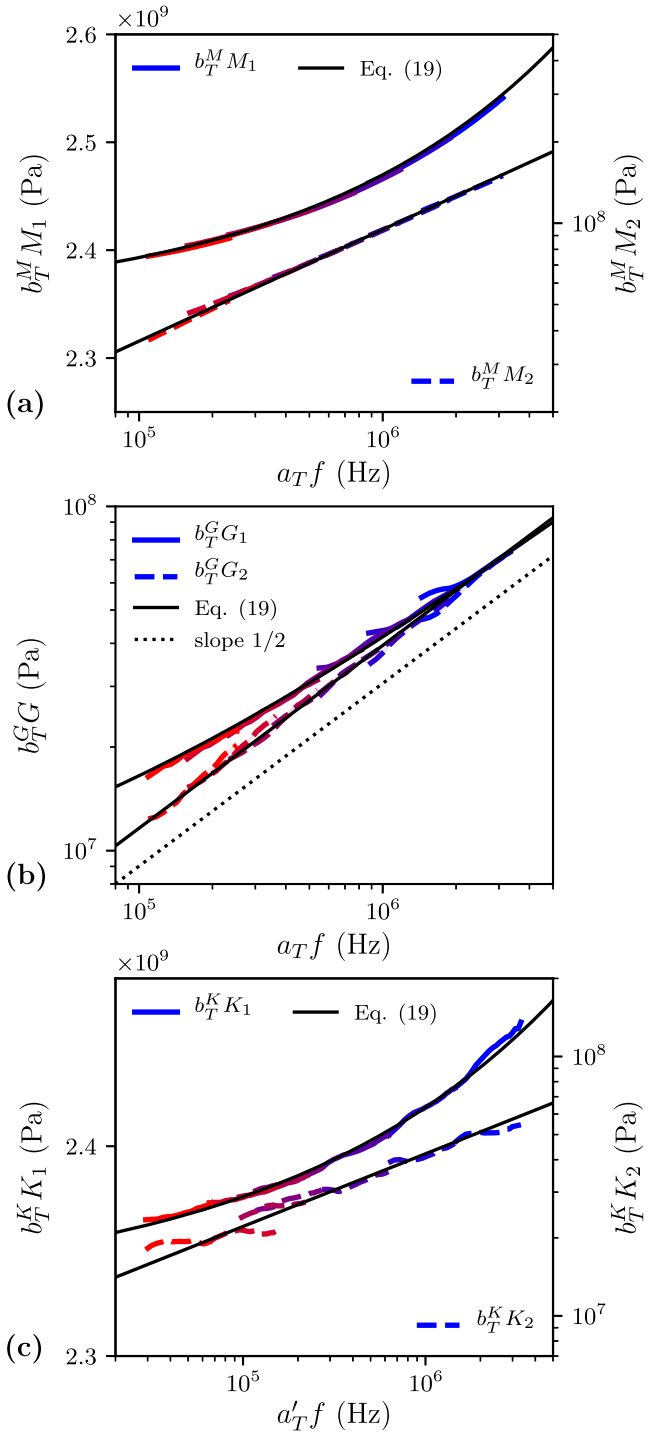

Fig. 13. (a) Variations in log–log scales of scaled storage and loss moduli versus scaled frequency with $T_{\text{ref}} = 5.1$ °C: (a) Longitudinal modulus $b_T^M M_1$ (solid lines, left-hand vertical scale) and $b_T^M M_2$ (dashed lines, right-hand vertical scale) versus $a_T f$ for several temperatures T_i^M, $i = 1$ to 8 (same color convention as in Fig. 9(a)). (b) Shear modulus $b_T^G G_1$ (solid lines) and $b_T^G G_2$ (dashed lines) versus $a_T f$ for several temperatures T_i^G, $i = 1$ to 7 (same color convention as in Fig. 11(a)). Black dotted curve: power-law with exponent 1/2. (c) Bulk modulus $b_T^K K_1$ (solid lines, left-hand vertical scale) and $b_T^K K_2$ (dashed lines, right-hand vertical scale) versus $a'_T f$ for several temperatures T_i^M, $i = 1$ to 7. Black solid curves: best fit by Eq. (19).

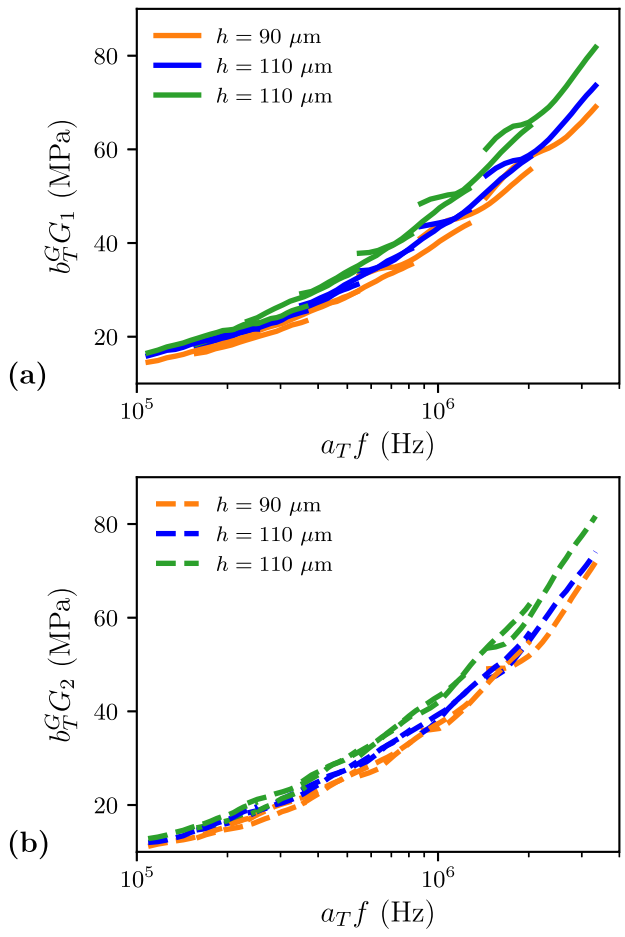

Fig. A.14. Variations of (a) scaled storage shear modulus $b_T^G G_1$ and (b) scaled loss shear modulus $b_T^G G_2$ versus scaled frequency $a_T f$ that were measured twice on one 110 µm-thick sample and on one 90 µm-thick sample with $T_{ref} = 5$ °C.

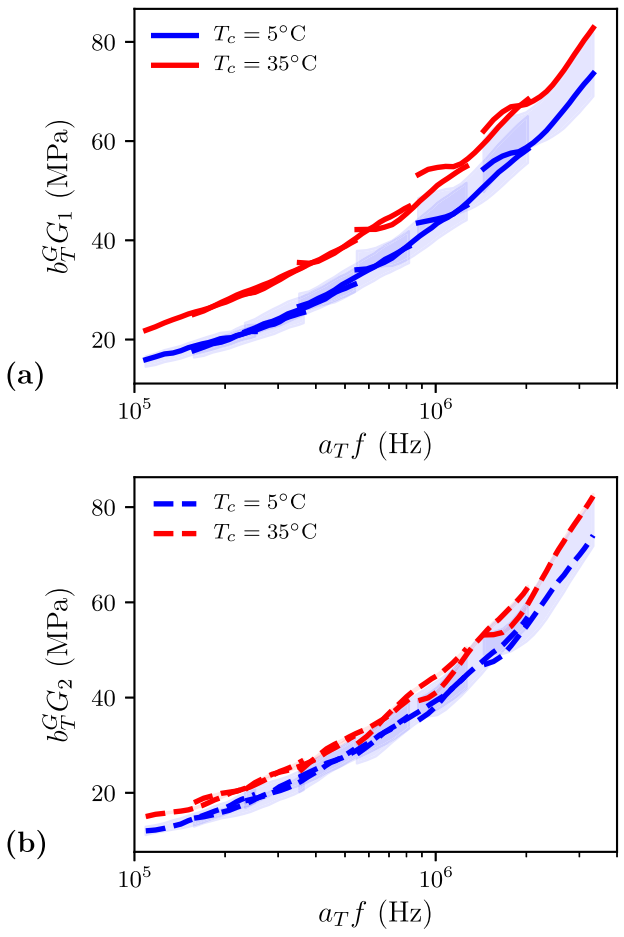

Fig. B.15. Variations of (a) scaled storage shear modulus $b_T^G G_1$ (solid lines) and (b) scaled loss shear modulus $b_T^G G_2$ (dashed lines) versus scaled frequency $a_T f$ with $T_{ref} = 5$ °C of two different 110 µm-thick samples hardened at two different temperatures $T_c = 5$ °C (blue lines) and $T_c = 35$ °C (red lines). Excess thickness represents the scatter associated to repeatability tests.

Declaration of competing interest

The authors declare the following financial interests/personal relationships which may be considered as potential competing interests: Baudis reports financial support was provided by French Government Defense Innovation Agency.

Data availability

Data will be made available on request.

Acknowledgments

The authors are grateful to Jean-Marie Citerne for his valuable assistance in the design and manufacturing of the sandwich technique. Q.B. acknowledges financial support of Agence Innovation Défense, France (AID).

Appendix A. Repeatability

In this appendix, we quantify the repeatability of the experiments.

On the one hand, as shown in Fig. 2, the discrepancy between the determinations of c_L and α_L from two different samples is of the order of 0.5% regarding c_L and 5.0% regarding α_L. We do not go further into this concern since the immersion technique is standard.

On the other hand, as shown in Fig. A.14, the discrepancy between the determinations of G_1 and G_2 from three different experiments (entailing two samples with the same thickness, namely 110 µm, and one 90 µm-thick sample) is of the order of 12–16% and increases with frequency.

Appendix B. Influence of the hardening temperature

In this appendix, we evaluate the influence of the hardening temperature on PU rheological properties.

Regarding M, cross-linking was performed at two different temperatures, namely 25 °C and 80 °C. No effect of the hardening temperature on c_L and α_L could be measured.

Regarding G, cross-linking was performed at two different temperatures, namely $T_c = 5$ °C and $T_c = 35$ °C. As shown in Fig. B.15, G_1 and G_2 markedly depend on T_c, i.e. their sensitivity to T_c is larger than the scatter associated to the lack of repeatability of the measurement technique. We conclude that the cross-linking temperature has a noticeable effect on G. This demonstrates the importance of temperature control during the hardening process.

Appendix C. Monitoring of the hardening process

The hardening kinetics of cross-linking polymers can be monitored using ultrasound, see [51,52] and references therein. For hard polymers such that $K \simeq G$, the variations of G can be accessed through M. Consequently, their hardening can be monitored using longitudinal

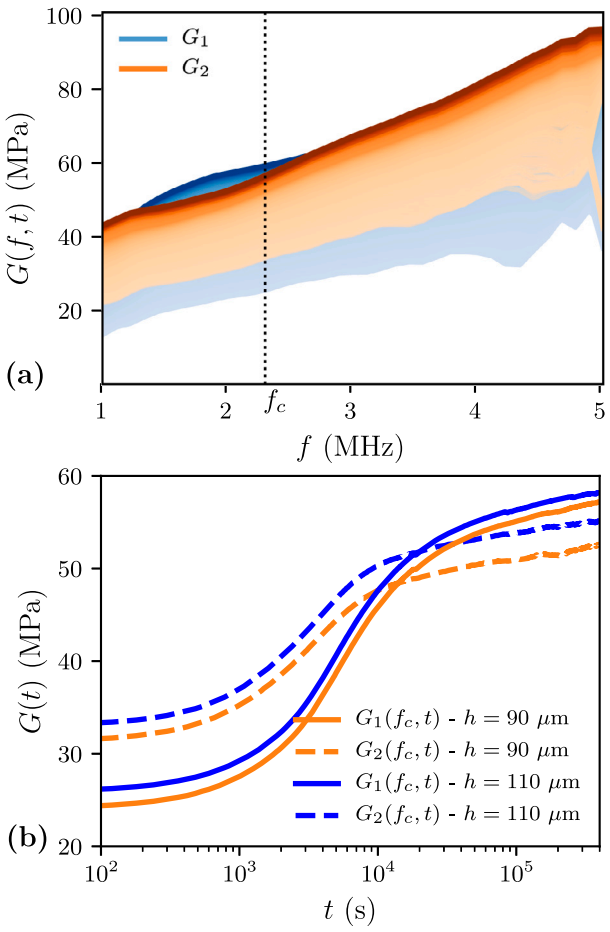

Fig. C.16. (a) Temporal evolutions of storage and loss shear moduli at frequency f_c during the cross-linking process occurring at temperature $T_c = 5$ °C of a $h = 110$ µm sample. The darker the curve, the later its acquisition time. (b) Temporal evolutions of storage and loss shear moduli at frequency f_c during the cross-linking process occurring at temperature $T_c = 5$ °C of two samples with different thicknesses $h = 90$ µm and $h = 110$ µm.

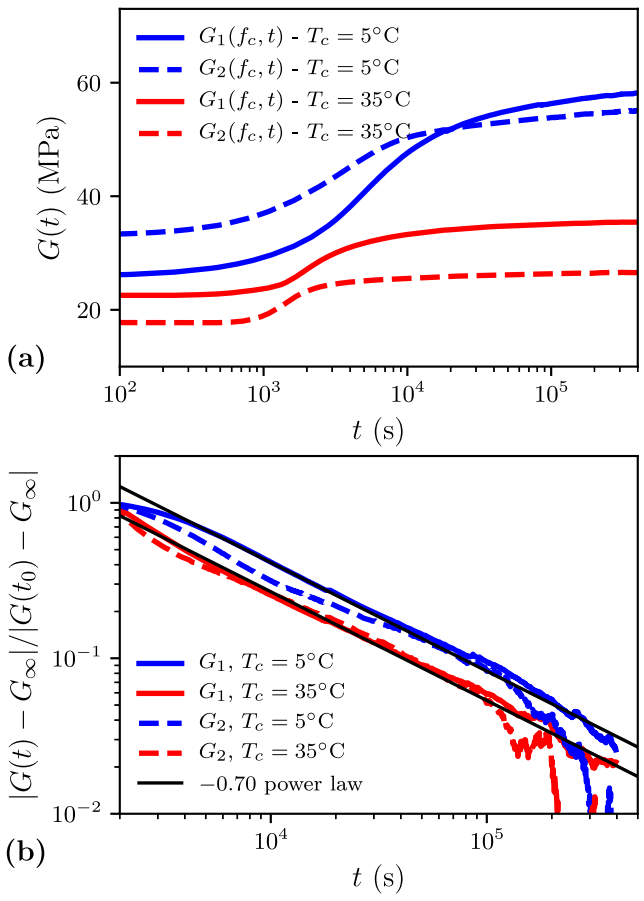

Fig. C.17. (a) Temporal evolution of storage and loss shear moduli at frequency f_c during the cross-linking process occurring at two different temperatures $T_c = 5$ °C and $T_c = 35$ °C. (b) Temporal evolution in log–log scales of the dimensionless deviation of G_1 (resp. G_2) from its final value $G_{1\infty}$ (resp. $G_{2\infty}$) during the cross-linking process occurring at two different temperatures $T_c = 5$ °C and $T_c = 35$ °C ($t_0 = 10^3$ s).

waves. For soft materials such that $G \ll K$, hardening has a little effect on M, so that its monitoring using longitudinal waves is not relevant.

The hardening of cross-linking polymers could also be directly monitored using shear waves [53,54], provided that their attenuation is not too large. In this appendix, we show how the setup used to measure the transverse velocity and attenuation of cross-linked PU samples can also be used to monitor the PU hardening process, more precisely to *a posteriori* evaluate the evolution of PU shear modulus during this process.

For this purpose, during the hardening process that occurs at controlled temperature T_c, the reflected and transmitted signals are acquired on a regular basis. They are observed to evolve in time during this process. When they do not evolve anymore, the PU hardening process is assumed as achieved, the last acquired signals are considered as the steady-state signals, the setup is unmounted and the calibration signals are acquired at the same temperature.

Given Eq. (6), the shear modulus of the hardening PU at time t can be determined using the following expression of the Fourier transform of the square of the transmission coefficient measured at time t, $(\mathcal{T}^{\text{exp}})^2(\omega,t)$:

$$(\mathcal{T}^{\text{exp}})^2(\omega,t) = (\mathcal{T}^{\text{exp}})^2_{\text{final}} \frac{\hat{S}(\omega,t)}{\hat{S}_{\text{final}}(\omega)} \tag{C.1}$$

where $(\mathcal{T}^{\text{exp}})^2_{\text{final}}$ is the steady-state signal. Fig. C.16(a) displays the time evolution of G during the hardening at $T_c = 5$ °C of a $h = 110$ µm thick sample. We note the increase in time of G_1 and G_2 and the appearance of a plateau for G_1 at low frequencies, which can be ascribed to PU hardening. Fig. C.16(b) displays the time evolution of G at central frequency f_c during the hardening at $T_c = 5$ °C of two samples with different thicknesses, namely $h = 90$ µm and $h = 110$ µm. We note that the variation of G during the cross-linking process is marked and noise-free. More precisely, both G_1 and G_2 increase in time with a steep evolution after about one hour of hardening. The jump of G_1 can be interpreted as the transition of PU from liquid behavior to solid behavior. Besides, the absence of trend in the variation of G with h demonstrates the independence of the cross-linking kinetics regarding h, which indicates that these thin samples do not undergo any noticeable self-heating during the cross-linking reaction and that the reaction is not affected by noticeable finite-size effect. This demonstrates that this technique can be actually used to monitor a bulk cross-linking reaction and allows to foresee a parametric, quantitative monitoring of the hardening kinetics using shear waves.

Fig. C.17(a) displays the time evolution of G at frequency f_c during the hardening at two different temperatures $T_c = 5$ °C and $T_c = 35$ °C. We observe that the larger T_c, the earlier the inflection of the $G_1(t)$ and $G_2(t)$ curves occurs. This is in agreement with the empirical observation that PU hardening is activated by temperature [37].

More precisely, Fig. C.17(b) displays the temporal evolution of the dimensionless deviation of G_1 (resp. G_2) at frequency f_c from its final value $G_{1\infty}$ (resp. $G_{2\infty}$) at late times during the cross-linking process occurring at two different temperatures $T_c = 5$ °C and $T_c = 35$ °C. We

note that these quantities evolve as power laws of time with exponent −0.70, indicating a long transient toward complete hardening.

References

[1] D.M. Crawford, J.A. Escarsega, Dynamic mechanical analysis of novel polyurethane coating for military applications, Thermochim. Acta 357–358 (2000) 161–168.
[2] C. Roland, Naval applications of elastomers, Rubber Chem. Technol. 77 (2004).
[3] R.N. Capps, I.J. Bush, S.T. Lieberman, S.E. Eveland, Evaluation of environmental effects on candidate polymeric materials for underwater optoacoustic sensors, Ind. Eng. Chem. Prod. Res. Dev. 21 (4) (1982).
[4] R. Capps, Elastometric Materials for Acoustical Applications, Naval Research Laboratory, Washington DC, 1989.
[5] P.H. Mott, C.M. Roland, R.D. Corsaro, Acoustic and dynamic mechanical properties of a polyurethane rubber, J. Acoust. Soc. Am. 111 (4) (2002) 1782–1790.
[6] C. Audoly, Acoustic metamaterials and underwater acoustics applications, in: Fundamentals and Applications of Acoustic Metamaterials: From Seismic to Radio Frequency, Vol. 1, 2019, pp. 263–285.
[7] I. Ward, Mechanical Properties of Solid Polymers, third ed., Wiley, 2003.
[8] R.S. Lakes, Viscoelastic measurement techniques, Rev. Sci. Instrum. 75 (4) (2004) 797–810.
[9] M. Williams, R. Landel, J. Ferry, The temperature dependence of relaxation mechanisms in amorphous polymers and other glass-forming liquids, J. Am. Chem. Soc. 77 (1955) 3701–3707.
[10] R. Capps, Dynamic Young's moduli of some commercially available polyurethanes, J. Acoust. Soc. Am. 73 (6) (1983).
[11] B. Hartmann, G.F. Lee, Dynamic mechanical relaxation in some polyurethanes, J. Non-Crystalline Solids 131–133 (1991) 887–890.
[12] D. Ionita, M. Cristea, C. Gaina, Prediction of polyurethane behaviour via time-temperature superposition: Meanings and limitations, Polym. Test. 83 (2020) 106340.
[13] I. Alig, S. Tadjbakhsch, A. Zosel, Comparison of ultrasonic shear wave and dynamic-mechanical measurements in acrylic-type copolymers, J. Polym. Sci. B 36 (10) (1998) 1703–1711.
[14] W. Sachse, Y.-H. Pao, On the determination of phase and group velocities of dispersive waves in solids, J. Appl. Phys. 48 (1978) 4320.
[15] R. Kline, Measurement of attenuation and dispersion using an ultrasonic spectroscopy technique, J. Acoust. Soc. Am. 76 (2) (1984) 498–504.
[16] N. Samet, P. Maréchal, H. Duflo, Ultrasonic characterization of a fluid layer using a broadband transducer, Ultrasonics 52 (3) (2012) 427–434.
[17] T. Norisuye, S. Sasa, K. Takeda, M. Kohyama, Q. Tran-Cong-Miyata, Simultaneous evaluation of ultrasound velocity, attenuation and density of polymer solutions observed by multi-echo ultrasound spectroscopy, Ultrasonics 51 (2) (2011) 215–222.
[18] K. Tsuji, T. Norisuye, H. Nakanishi, Q. Tran-Cong-Miyata, Simultaneous measurements of ultrasound attenuation, phase velocity, thickness, and density spectra of polymeric sheets, Ultrasonics 99 (2019) 105974.
[19] J. Qiao, A.V. Amirkhizi, K. Schaaf, S. Nemat-Nasser, G. Wu, Dynamic mechanical and ultrasonic properties of polyurea, Mech. Mater. 43 (10) (2011) 598–607.
[20] Z. Jia, A.V. Amirkhizi, W. Nantasetphong, S. Nemat-Nasser, Experimentally-based relaxation modulus of polyurea and its composites, Mech. Time-Dependent Mater. 20 (2) (2016) 155–174.
[21] L. Brinson, H. Brinson, Polymer Engineering Science and Viscoelasticity: An Introduction, second ed., Springer US, 2015.
[22] J. Wu, Determination of velocity and attenuation of shear waves using ultrasonic spectroscopy, J. Acoust. Soc. Am. 99 (5) (1996) 2871–2875.
[23] B. Hartmann, J. Jarzynski, Immersion apparatus for ultrasonic measurements in polymers, J. Acoust. Soc. Am. 56 (5) (1974) 1469–1477.
[24] V.C. Camara, D. Laux, O. Arnould, Enhanced multiple ultrasonic shear reflection method for the determination of high frequency viscoelastic properties, Ultrasonics 50 (7) (2010) 710–715.
[25] O. Manfredi, R. Mills, M. Schirru, R. Dwyer-Joyce, Non-invasive measurement of lubricating oil viscosity using an ultrasonic continuously repeated chirp shear wave, Ultrasonics 94 (2019) 332–339.
[26] A. Rabbani, D.R. Schmitt, Ultrasonic shear wave reflectometry applied to the determination of the shear moduli and viscosity of a viscoelastic bitumen, Fuel 232 (2018) 506–518.
[27] E.E. Franco, H.M. Barrera, P.O. Formigoni, F. Buiochi, Shear-wave corner retroreflector device for ultrasonic measurement of viscosity, Ultrasonics 117 (2021) 106538.
[28] M.S. Greenwood, J.D. Adamson, L.J. Bond, Measurement of the viscosity–density product using multiple reflections of ultrasonic shear horizontal waves, Ultrasonics 44 (2006) e1031–e1036.
[29] P. Longin, C. Verdier, M. Piau, Dynamic shear rheology of high molecular weight polydimethylsiloxanes: Comparison of rheometry and ultrasound, J. Non-Newt. Fluid Mech. 76 (1998) 213–232.
[30] I. Alig, D. Lellinger, J. Sulimma, S. Tadjbakhsch, Ultrasonic shear wave reflection method for measurements of the viscoelastic properties of polymer films, Rev. Sci. Instrum. 68 (3) (1997) 1536–1542.
[31] M. Thieury, Développement De Métamatériaux Super-Absorbants Pour L'acoustique Sous-Marine (Ph.D. thesis), Université Paris sciences et lettres, 2020.
[32] W.N. Bodé, F. Lickert, P. Augustsson, H. Bruus, Determination of the complex-valued elastic moduli of polymers by electrical-impedance spectroscopy for ultrasound applications, Phys. Rev. A 18 (6) (2022) 064078.
[33] G. Lefebvre, R. Wunenburger, T. Valier-Brasier, Ultrasonic rheology of visco-elastic materials using shear and longitudinal waves, Appl. Phys. Lett. 112 (2018) 241906.
[34] L.E. Kinsler, A.R. Frey, A.B. Coppens, J.V. Sanders, Fundamentals of Acoustics, fourth ed., John Wiley and Sons, 2009.
[35] D. Royer, T. Valier-Brasier, Elastic Waves in Solids 1. Propagation, Vol. 1, Wiley-ISTE, 2022.
[36] F.E. Jones, G.L. Harris, ITS-90 density of water formulation for volumetric standards calibration, J. Res. Natl. Inst. Stand. Technol. 97 (3) (1992) 335.
[37] [link]. URL https://www.sf-composites.com/SpacePrivate/AXSUR34401_FT.pdf.
[38] T. Valier-Brasier, D. Royer, Elastic Waves in Solids 2. Radiation, Scattering, Generation, Vol. 2, Wiley-ISTE, 2022.
[39] J. Cheeke, Fundamental and Applications of Ultrasonic Waves, first ed., CRC Press, Bocat Raton, FL, 2002.
[40] A. Simon, G. Lefebvre, T. Valier-Brasier, R. Wunenburger, Viscoelastic shear modulus measurement of thin materials by interferometry at ultrasonic frequencies, J. Acoust. Soc. Am. 146 (5) (2019) 3131–3140.
[41] J. Luo, Z. Xie, X. Li, Asymmetric windows and their application in frequency estimation, J. Algorithms Comput. Technol. 9 (4) (2015) 389–412.
[42] J. Ferry, Viscoelastic Properties of Polymers, second ed., Willey, 1980.
[43] R. Christensen, Theory of Viscoelasticity, second ed., Dover Publications Inc., 2003.
[44] P.E. Rouse Jr., A theory of the linear viscoelastic properties of dilute solutions of coiling polymers, J. Chem. Phys. 21 (7) (1953) 1272–1280.
[45] F. Bueche, The viscoelastic properties of plastics, J. Chem. Phys. 22 (1954) 603–609.
[46] M. Doi, S. Edwards, Dynamics of concentrated polymer systems. Part 3.—The constitutive equation, J. Chem. Soc. Faraday Trans. 2: Mol. Chem. Phys. 74 (1978) 1818–1832.
[47] J. Dealy, D. Plazek, Time-temperature superposition—A users guide, Rheol. Bull 78 (2) (2009) 16–31.
[48] R.F. Landel, Mechanical properties of a polyurethane elastomer in the rubber-to-glass transition zone, J. Colloid Sci. 12 (3) (1957) 308–320.
[49] A.N. Norris, An inequality for longitudinal and transverse wave attenuation coefficients, J. Acoust. Soc. Am. 141 (1) (2017) 475–479.
[50] R.L. Bagley, P. Torvik, A theoretical basis for the application of fractional calculus to viscoelasticity, J. Rheol. 27 (3) (1983) 201–210.
[51] N. Ghodhbani, P. Maréchal, H. Duflo, Ultrasound monitoring of the cure kinetics of an epoxy resin: Identification, frequency and temperature dependence, Polym. Test. 56 (2016) 156–166.
[52] F. Lionetto, A. Maffezzoli, Monitoring the cure state of thermosetting resins by ultrasound, Materials 6 (9) (2013) 3783–3804.
[53] A.W. Chow, J.L. Bellin, Simultaneous acoustic wave propagation and dynamic mechanical analysis of curing of thermoset resins, Polym. Eng. Sci. 32 (3) (1992) 182–190.
[54] S. Dixon, B. Lanyon, Phase change measurement of ultrasonic shear waves on reflection from a curing epoxy system, J. Phys. D: Appl. Phys. 38 (22) (2005) 4115.